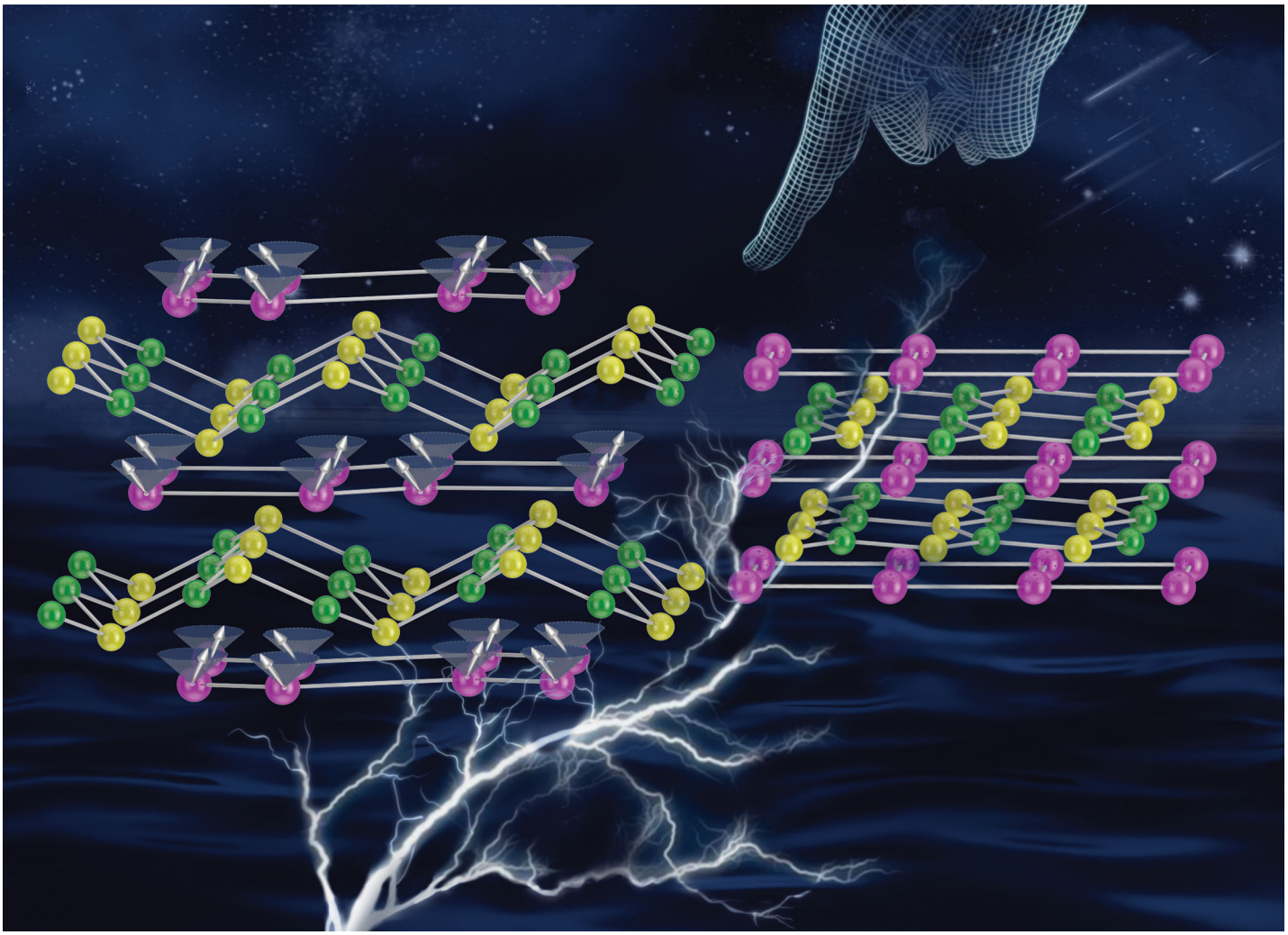

Showcasing research from Professors Fengxia Hu, Lunhua He, Baogen Shen and Dr Jing Wang at the Institute of Physics, Chinese Academy of Sciences, P. R. China.

Cone-spiral magnetic ordering dominated lattice distortion and giant negative thermal expansion in Fe-doped MnNiGe compounds

Negative thermal expansion (NTE) has emerged as a topic of intense research. By utilizing large lattice distortion caused by cone-spiral magnetic ordering and the induced texture effect, giant NTE exceeding the average crystallographical contribution has been achieved. This work provides a new strategy for exploring adjustable NTE behaviour.

As featured in:

See Fengxia Hu, Jing Wang, Lunhua He, Baogen Shen *et al.*, *Mater. Horiz.*, 2020, **7**, 804.

ROYAL SOCIETY OF CHEMISTRY

rsc.li/materials-horizons

Registered charity number: 207890

Materials Horizons

ROYAL SOCIETY OF CHEMISTRY

COMMUNICATION

View Article Online
View Journal | View Issue

Cite this: *Mater. Horiz.*, 2020, 7, 804

Received 8th October 2019,
Accepted 25th November 2019

DOI: 10.1039/c9mh01602c

rsc.li/materials-horizons

Cone-spiral magnetic ordering dominated lattice distortion and giant negative thermal expansion in Fe-doped MnNiGe compounds†

Feiran Shen,‡[abc] Houbo Zhou,‡[ab] Fengxia Hu,*[abd] Jian-Tao Wang,[abd] Sihao Deng,[c] Baotian Wang,[c] Hui Wu,[e] Qingzhen Huang,[e] Jing Wang,*[abf] Jie Chen,[c] Lunhua He,*[acd] Jiazheng Hao,[a] Zibing Yu,[ab] Feixiang Liang,[ab] Tianjiao Liang,[c] Jirong Sun[acd] and Baogen Shen*[abd]

Negative thermal expansion (NTE) has emerged as one of the intense research topics to meet the demands of the precision industry for compensating positive thermal expansion (PTE) properties. The adjustment of the NTE behavior is the key for tailoring thermal expansion. Chemical modification and the particle size effect have been regarded as effective means to tune the NTE behavior, and the crystallographic contribution is usually the upper limit of NTE. Here, we reported a new way to tune the NTE behavior involving lattice distortion that is dominated by the magnetic structure in hexagonal MnM′Ge-based (M′:Ni,Co) alloys. The achieved maximal linear NTE reached $\Delta L/L \sim -23\,690 \times 10^{-6}$ ($\bar{\alpha} = -121.5 \times 10^{-6}$ K^{-1}) in a temperature interval as wide as ~195 K (80–275 K) for Fe-doped MnNiGe alloys. This value was 3.3 times larger than that of the corresponding average crystallographical contribution and exceeded that of almost all NTE materials reported to date. Neutron powder diffraction and first-principles calculations were carried out. The results revealed that Fe-doped MnNiGe showed incommensurate cone-spiral magnetic ordering, and the lattice distortion during the phase transition was more significant than that of MnCoGeIn with linear ferromagnetic ordering. The larger lattice distortion favored the cleavage of the hexagonal phase along the *c*-axis. As a result, a texture effect along the (110) crystal plane occurred during the molding process, which greatly enhanced the amplitude of the isotropic in-plane linear NTE.

New concepts

Negative thermal expansion (NTE) has emerged as one of the intense research topics. Chemical modification and the particle size effect have been regarded as effective means to tune the NTE behavior. However, the amplitude and temperature region of NTE are usually limited by the crystallographic contribution. Here, we report a new way to tune the NTE behavior, which involves the lattice distortion that is dominated by the magnetic structure in MnM′Ge-based (M′ = Ni, Co) alloys. The large lattice distortion caused by cone-spiral magnetic ordering in Fe-doped MnNiGe promotes cleavage and induces a texture effect, which greatly enhances NTE. The achieved maximal linear NTE is 3.3 times larger than that of the corresponding average crystallographical contribution and exceeds that of almost all the NTE materials reported to date. In contrast, the smaller lattice distortion in MnCoGeIn with linear FM ordering limits its texture forming ability, and the maximal NTE never exceeds the crystallographic contribution. This is the first time to tune the NTE behavior by relying on the lattice distortion dominated by the magnetic structure and the induced texture effect, which helps to break through the restriction of crystallographic contribution and achieves a giant NTE behavior. The present study provides a new strategy for exploring the adjustable NTE behavior.

The present study provides a new strategy for exploring adjustable NTE behaviors.

Introduction

It is well-known that most materials exhibit positive thermal expansion (PTE) properties. Although the length change caused by PTE is only 10^{-5} to 10^{-6}, this magnitude of change can greatly affect the performance of some devices or instruments, especially in some precision industrial fields, such as printed circuit boards, optical fiber reflective grating devices, and high-precision optical mirrors. The undesired PTE behavior of conventional materials can be effectively modified by mixing with a negative thermal expansion (NTE) material. Therefore, NTE has emerged as one of the intense research topics to meet the demands of the precision industry. However, the process of

[a] *Institute of Physics, Chinese Academy of Sciences, Beijing 100190, China. E-mail: fxhu@iphy.ac.cn, lhhe@iphy.ac.cn, wangjing@iphy.ac.cn, shenbg@iphy.ac.cn*
[b] *School of Physical Sciences, University of Chinese Academy of Sciences, Beijing 101408, China*
[c] *Spallation Neutron Source Science Center, Dongguan 523803, China*
[d] *Songshan Lake Materials Laboratory, Dongguan, Guangdong 523808, China*
[e] *NIST Center for Neutron Research, National Institute of Standards and Technology, Gaithersburg, Maryland 20899, USA*
[f] *Fujian Innovation Academy, Chinese Academy of Sciences, Fuzhou, Fujian 350108, China*

† Electronic supplementary information (ESI) available: Sample preparation, characterization, computational method, magnetic and crystal structure analysis, first-principles calculations, texture analysis, and supplementary table and figures. See DOI: 10.1039/c9mh01602c

‡ These authors contribute equally to this work.

making precise devices usually needs a good match in the coefficient of thermal expansion (CTE) values between different components. The adjustment of the NTE behavior, which includes the amplitude and the temperature region of NTE, becomes the key in NTE research. Currently, chemical modification has been regarded as an effective method to tune the NTE behavior in many NTE materials,[1] such as ZrW_2O_8-based compounds,[2–4] ScF_3-based compounds,[5,6] $PbTiO_3$-based compounds,[7–9] antiperovskite manganese nitrides,[10–14] $La(Fe,Si)_{13}$-based compounds,[15,16] cubic Laves phase $Tb(Co,Fe)_2$[17] and $BiNO_3$.[18] Additionally, the particle size effect can control the thermal expansion behavior through interface effects or defects in some cases, such as CuO,[19] $PbTiO_3$–$BiFeO_3$ perovskite,[20] antiperovskite $Mn_3Cu_{0.5}Ge_{0.5}N$,[21] PtNi,[22] semimetal bismuth,[23] TiO_2[24] and ScF_3.[25] Although the NTE behavior can be tuned by these two methods, the amplitude and temperature region of NTE is normally limited by crystallographic contribution irrespective of whether the dominated mechanism is a phonon-induced type,[2–6,23–25] such as a tension effect, or an electronic transition-induced one, such as a magnetic, ferroelectric, or charge order.[7–22] In other words, it is hard to obtain NTE that exceeds lattice contribution. One exception is the giant NTE reported recently in the reduced layered ruthenate.[26,27] The maximal linear thermal expansion, $\Delta L/L \sim 22\,333 \times 10^{-6}$, largely exceeds the crystallographic contribution during the Mott metal–insulator phase transition. The cause of this is related to the change in elastic properties and morphology by the reduction of oxygen.[27]

Ternary metallic compounds MM′X (M, M′ = transition element, X = main element) with the proper components undergo a martensitic structural transition from hexagonal Ni_2In-type austenite (space group $P6_3/mmc$) to TiNiSi-type orthorhombic martensite (space group *Pnma*) upon cooling. During the transition, the hexagonal lattice expands along the *c*-axis (c_H) and contracts along the *a*-axis (a_H), accompanied with significant anisotropic unit-cell volume expansion.[28] Hence, these types of materials provide an excellent platform for exploring the novel performance of NTE. For instance, *via* bonding polycrystalline powders and introducing residual stress to impact the phase transition,[29] isotropic NTE with a linear expansion as large as $\Delta L/L \sim -10\,213 \times 10^{-6}$ (~93% of the crystallographic value $\Delta V/V = -3.9\%$[30]) in a wide temperature range was obtained in MnCoGe-based compounds, which surpassed the performance of most NTE materials.

For the MM′X (M = Mn) alloys, austenite usually displays ferromagnetic (FM) properties, but various magnetic ground states appear in martensite. During the phase transition, the arrangement of Mn atoms (the main carriers of the magnetic moment) changes from a straight alignment in austenite to polygonal chains in martensite (Fig. 1a and b). The interatomic distances between the adjacent Mn atoms (d_1, d_2) therefore change[31] (Fig. S1 in the ESI†), resulting in rich magnetic ground states in martensite because the magnetic coupling is extremely sensitive to the Mn–Mn interatomic distances.[32,33] For example, stoichiometric MnNiGe[34] and MnCoGe[35] display antiferromagnetic (AFM) and FM natures in martensite, respectively, where the only difference is the element in the M′ site, *i.e.*, Co and Ni, which are neighbors in the periodic table and have almost the same atomic radius. However, the lattice symmetry and interatomic distances of MnCoGe and MnNiGe are pronouncedly affected by their distinct magnetic couplings.

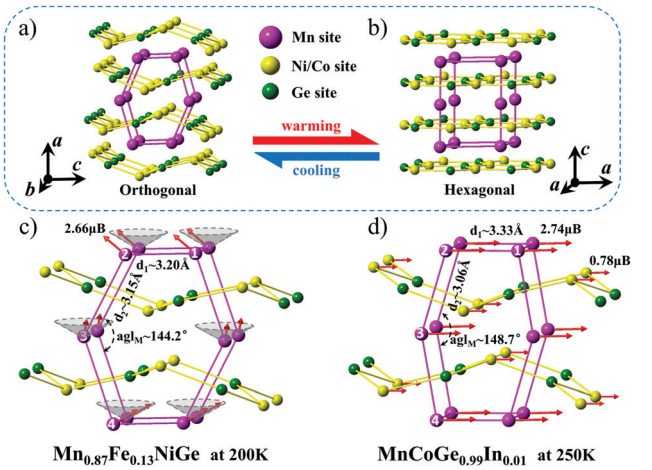

Fig. 1 (a and b) Sketches of orthorhombic and hexagonal structures of MnNiGe/MnCoGe, where the change of unit cell (magenta lines enclosed) and atomic chains can be clearly identified. (c and d) Fragments of the cone-spiral magnetic structure ($Mn_{0.87}Fe_{0.13}NiGe$) and linear FM ($MnCoGe_{0.99}In_{0.01}$) structures viewed along the *b* axes with selected distances labeled in Å, the Mn1–Mn2 distance d_1 along the *c*-axis, the Mn2–Mn3 distance d_2, and the angle agl_M of the Mn2–Mn3–Mn4 atomic chain are indicated.

Stoichiometric MnNiGe shows a martensitic structural transition around $T_S \sim 420$ K, and martensite displays a spiral AFM structure with a Neél temperature T_N at ~356 K.[34] By optimizing the composition, concurrent magnetic and structural transitions emerge when either the Mn or Ni site is substituted by Fe;[36] hence, a giant magnetocaloric effect (MCE) has been reported. Although the negative expansion during a phase transition (such as $\Delta V/V \sim -2.68\%$ for $Mn_{0.86}Ni_{0.14}FeGe$)[36] is smaller than that of the MnCoGe-based alloys ($\Delta V/V \sim -3.9\%$ for $MnCoGe_{0.99}In_{0.01}$),[30] our neutron studies reveal that Fe-doped MnNiGe with a cone-spiral magnetic structure shows a larger change in lattice distortion than MnCoGeIn with a linear FM structure during the transition (Fig. S2, ESI†). The large lattice distortion favors cleavage during the pulverization process; hence, a strong texture can be produced under pressure during the molding process. By utilizing the magnetic structure controlled lattice distortion, giant NTE is achieved in Fe-doped MnNiGe. The maximal linear expansion reaches $\Delta L/L \sim -23\,690 \times 10^{-6}$ in a wide temperature window of 195 K (80–275 K), which exceeds the performance of almost all other NTE materials reported to date.

Results and discussion

Fe-Doped MnNiGe alloys were synthesized by means similar to those reported in ref. 29 (ESI I†). To characterize the magnetic structure and lattice symmetry during the phase transition, we performed variable temperature neutron powder diffraction (NPD) studies for $Mn_{1-x}Fe_xNiGe$ (x = 0.11, 0.13) and X-ray diffraction (XRD) for $MnNi_{1-y}Fe_yGe$ (y = 0.2, 0.23) and

$Mn_{1-x}Fe_xNiGe$ (x = 0.09) (ESI II†). The refined results are given in Table S1 (ESI†) together with those of $MnCoGe_{0.99}In_{0.01}$.[30] The NPD refinements indicated that a spiral-type incommensurate magnetic structure existed with the spiral axis parallel to the a-axis for martensite of $Mn_{0.87}Fe_{0.13}NiGe$. The magnetic reflections were indexed by the propagation vector k = [0.17357(3), 0, 0]. The magnetic moment localized on Mn sites with μ(Mn, Fe) = 2.66(1) μ_B, and the angle from the a-axis was 70° at 200 K, showing a canted FM nature (here, we assume that Fe and Mn randomly occupy the same sites). In contrast, $MnCoGe_{0.99}In_{0.01}$ with Co showed a linear FM structure in martensite with μ(Mn) = 2.74(5) μ_B and μ(Co) = 0.78(6) μ_B at 250 K (please see Fig. 1c and d and the details in Table S1, ESI†).

For such TiNiSi-type martensites, the magnetic structure resulted from the competition between the direct exchange of Mn1–Mn2 (d_1) and superexchange of Mn2–Mn3 (d_2) (Fig. 1c and d), where the former plays a dominant role.[32,33,37] Density functional theory (DFT)[32,33] calculations revealed that the magnetic ground state critically depended on the d_1 length. For $d_1 \leq 2.5$ Å, the close distance between the Mn atoms led to a strong overlap of the 3d orbitals, and no magnetic ground state was stable due to the broad 3d hybrid bands. As the d_1 length increased, the overlap of the 3d orbitals of Mn became smaller, resulting in more localized 3d electrons and enhanced exchange between the Mn atoms. For 2.5 Å $\leq d_1 \leq$ 2.9 Å, the FM ground state showed lower energy, while for 2.9 Å $\leq d_1 \leq$ 3.3 Å, the AFM state showed lower energy. On further increasing the d_1 length to $d_1 \geq$ 3.3 Å, the FM state prevailed again. These calculations were experimentally verified by several members of the MM′X family, such as MnNiSi (FM, d_1 = 2.78 Å),[37] MnCoP (FM, d_1 = 2.88 Å),[32] MnNiGe (AFM, d_1 = 3.20 Å),[34] and MnCoGeIn (FM, d_1 = 3.33 Å, Fig. 1d).[30] However, during calculations, a collinear magnetic structure was considered.[32,33]

To demonstrate the stability of the spiral AFM structure in a MnNiGe alloy, we constructed a collinear AFM model and a spiral AFM model with a six unit cell period along the a-axis based on the NPD data. The total energy was calculated by first-principles calculations with PW91 generalized gradient approximation[38,39] (see Computational details given in ESI I†). The results (Fig. 2a) indicate that the total energy of the spiral AFM structure (−78.557 eV f.u.$^{-1}$) is lower than that of the collinear AFM (−78.272 eV f.u.$^{-1}$), suggesting that the spiral AFM ground state is more stable for MnNiGe.

For the present $Mn_{0.87}Fe_{0.13}NiGe$, d_1 is 3.20 Å; it is the same as those in stoichiometric MnNiGe,[34] which should favour the spiral AFM coupling. However, the substitution of Mn with Fe introduces FM coupling in Fe–6Mn configurations,[36] which can help establish cone-spiral magnetic coupling. To confirm the stability of the cone-spiral magnetic structure in $Mn_{0.87}Fe_{0.13}NiGe$, we further calculated the total energy in both the cone-spiral state and spiral AFM state, where the atomic position, *i.e.*, structural symmetry refined from the NPD data was taken into account. The energy difference ($\Delta E = E_{\text{cone-spiral}} - E_{\text{spiral-AFM}}$) per formula unit is plotted in Fig. 2b with an isotropic lattice strain change from −5% to +5%, which is related to the experimental lattice parameters. The results indicate that the cone-spiral magnetic state is more stable than the spiral AFM, showing

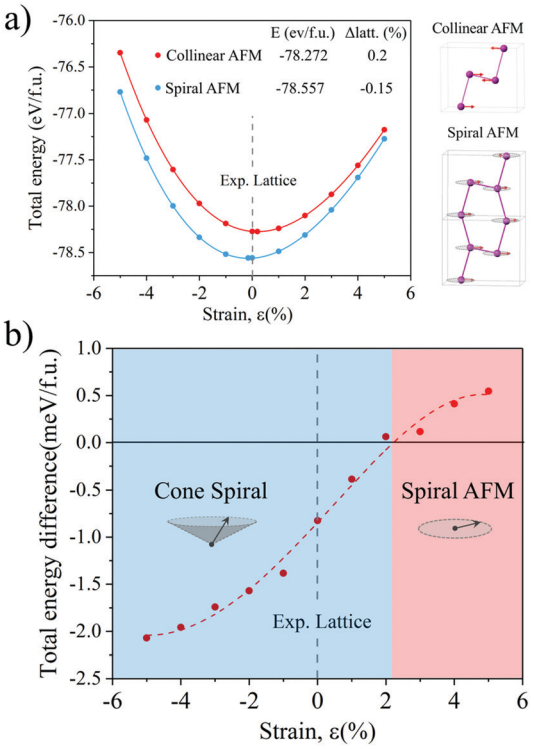

Fig. 2 (a) Total energy per formula unit of the MnNiGe as a function of the lattice strain for the spiral AFM and collinear AFM states. Right panel shows the sketches of the collinear AFM and spiral AFM magnetic structures. (b) Difference between the total energies of cone-spiral and spiral AFM states in $Mn_{0.87}Fe_{0.13}NiGe$ as a function of the lattice strain. The cone-spiral magnetic configuration becomes stable when $\Delta E < 0$.

an energy gain of 0.8 meV f.u.$^{-1}$ with the experimental lattice parameters (ε = 0%).

For the lattice distortion relative to the magnetic structure (Fig. 1c and d), we chose a representative composition $Mn_{0.87}Fe_{0.13}NiGe$ and compared it to $MnCoGe_{0.99}In_{0.01}$ with a linear FM structure. Due to the distinct magnetic coupling, the differences of d_1 and d_2 between the two alloys reach 3.61% and 2.60%, respectively, and the agl_M (144.3°) of the Mn2–Mn3–Mn4 atomic chain in $Mn_{0.87}Fe_{0.13}NiGe$ is smaller than that (148.6°) in $MnCoGe_{0.99}In_{0.01}$ by 2.89% (Fig. S1 and Table S1, ESI†). Hence, different lattice symmetries appear in martensite for the two alloys, which are evidently displayed in Fig. 1c and d. As seen from Table S1 (ESI†), d_1, d_2, and agl_M as well as the lattice parameters indicate that all the Fe-doped MnNiGe alloys show larger lattice distortions than $MnCoGe_{0.99}In_{0.01}$ during the martensitic transition.

To quantify the lattice distortion, we define a numeral parameter, Δ_{ani}, as follows:

$$\Delta_{ani} = \sqrt{\frac{1}{3}\cdot\left[(\Delta a/a - \Delta l/l)^2 + (\Delta b/b - \Delta l/l)^2 + (\Delta c/c - \Delta l/l)^2\right]} \quad (1)$$

Here, $\Delta a/a = (c_H - a_O)/c_H$, $\Delta b/b = (a_H - b_O)/b_O$, and $\Delta c/c = (a_H - c_O)/a_H$ denote the change ratio of lattice parameters across the transition between hexagonal (H) and orthorhombic (O) phases, and $\Delta l/l = (\Delta V/V)/3$ ($\Delta V/V$ represents the change in unit-cell volume). The

obtained Δ_{ani} values were 8.68%, 8.35%, 8.40%, 8.51%, and 8.27% for $Mn_{0.87}Fe_{0.13}NiGe$, $MnNi_{0.8}Fe_{0.2}Ge$, $MnNi_{0.77}Fe_{0.23}Ge$, $Mn_{0.91}Fe_{0.09}NiGe$, and $Mn_{0.89}Fe_{0.11}NiGe$, respectively (Table S1, ESI†), which showed similar cone-spiral magnetic structures (see details in ESI II and Fig. S3–S5, ESI†). In contrast, $MnCoGe_{0.99}In_{0.01}$ with a linear FM structure showed Δ_{ani} that was about 7.49%, which was smaller than those of Fe-doped MnNiGe by 12% on average. The larger lattice distortion motivates cleavage during the pulverization process, and a strong texture appears under pressure. As a result, NTE with giant linear $\Delta L/L$ is achieved in the Fe-doped MnNiGe alloys.

Fig. 3a shows the linear thermal expansion $\Delta L/L$ measured using a high-resolution strain gauge from 390 K down to 80 K for the bonded samples with different particle sizes. The $\Delta L/L$ behavior on the top surface of bonded pellet is isotropic in-plane (Fig. 3c). For $Mn_{0.87}Fe_{0.13}NiGe$, $MnNi_{0.8}Fe_{0.2}Ge$, $MnNi_{0.77}Fe_{0.23}Ge$, and $Mn_{0.91}Fe_{0.09}NiGe$, the particle sizes before bonding are 60–80 μm, 20–50 μm, 20–40 μm, and 10–20 μm (Fig. 3b), respectively, and the measured maximal $\Delta L/L$'s reach 23 690, 17 416, 16 172, and 9171 $\times 10^{-6}$ in the temperature intervals of 195 K (80–275 K), 162 K (180–342 K), 186 K (132–318 K), and 138 K (194–332 K); hence, the corresponding average linear NTE coefficients are $\bar{\alpha} \sim -121.5$, -107.5, -86.9, and -66.5×10^{-6} K^{-1} (Table S1, ESI†). Note that the measured $\Delta L/L \sim 23\,690 \times 10^{-6}$ for $Mn_{0.87}Fe_{0.13}NiGe$ did not reach the maximum at 80 K. This means that the actual $\Delta L/L$ should be larger. Even so, the maximal $\Delta L/L \sim 23\,690 \times 10^{-6}$ and the corresponding NTE coefficient $\bar{\alpha} \sim -121.5 \times 10^{-6}$ K^{-1} over a ~195 K interval exceeded that of almost all NTE materials reported previously. For example, these performances reach or even surpass $\Delta L/L \sim 22\,333 \times 10^{-6}$ and the maximal $\bar{\alpha} \sim 115 \times 10^{-6}$ K^{-1} (over the nearly equivalent interval of ~200 K) of the reduced layered ruthenate, the maximal NTE reported to date.[27] Moreover, the present $\Delta L/L \sim 23\,690 \times 10^{-6}$ is more than 2 times larger than that ($\Delta L/L \sim 10\,213 \times 10^{-6}$) of bonded $MnCoGe_{0.99}In_{0.01}$,[29] and the corresponding NTE coefficient $\bar{\alpha} \sim -121.5 \times 10^{-6}$ K^{-1} (over a 195 K interval) is also more than 2 times larger than that ($\bar{\alpha} \sim -51.5 \times 10^{-6}$ K^{-1} over a similar interval of ~210 K) of the bonded $MnCo_{0.98}Cr_{0.02}Ge$.[29] Such giant isotropic in-plane NTE in a wide temperature interval suggests the immense potential for compensating numerous materials with extremely high PTE, such as the widely used organic or plastic materials, whose PTE coefficients are up to 100–200 $\times 10^{-6}$ K^{-1}.

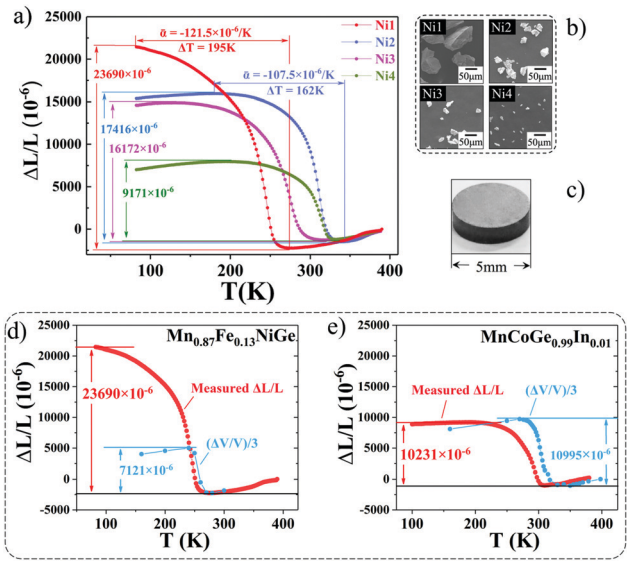

Fig. 3 (a) The measured linear thermal expansions $\Delta L/L$ for the bonded $Mn_{0.87}Fe_{0.13}NiGe$ (Ni1), $MnNi_{0.8}Fe_{0.2}Ge$ (Ni2), $MnNi_{0.77}Fe_{0.23}Ge$ (Ni3), and $Mn_{0.91}Fe_{0.09}NiGe$ (Ni4) with different particle sizes (the reference temperature is 390 K). (b) The SEM micrograph of particles before bonding. (c) The morphology of the bonded particles. The comparison between the measured $\Delta L/L$ and the calculated $(\Delta L/L)_0 = (\Delta V/V)/3$ for (d) $Mn_{0.87}Fe_{0.13}NiGe$ and (e) $MnCoGe_{0.99}In_{0.01}$.

To know the intrinsic crystallographic change during the phase transition, we performed variable temperature NPD or XRD measurements for these Fe-doped MnNiGe alloys before bonding. The refined results are shown in Fig. S6 and Table S1 (ESI†). The changes in lattice volume ($\Delta V/V \sim (2V_H - V_O)/2V_H$) during the phase transition at the corresponding same temperature points are −2.63%, −3.53%, −3.49%, and −2.66% for $Mn_{0.87}Fe_{0.13}NiGe$, $MnNi_{0.8}Fe_{0.2}Ge$, $MnNi_{0.77}Fe_{0.23}Ge$, and $Mn_{0.91}Fe_{0.09}NiGe$, respectively. If the lattice expansion was supposed to be isotropic for these polycrystalline samples, the linear $(\Delta L/L)_0 = (\Delta V/V)/3$ from the unit cell parameters would be 7121, 7473, 7626, and 7190 $\times 10^{-6}$ across the temperature intervals of 40 K (240–280 K), 35 K (295–330 K), 35 K (275–310 K), and 50 K (285–335 K), respectively (see ESI III and Table S1, ESI†). It is noticeable that the measured maximal $\Delta L/L$ values for the bonded samples were 3.3, 2.3, 2.1, and 1.3 times larger than those calculated $(\Delta L/L)_0$ from the crystallographic contribution for $Mn_{0.87}Fe_{0.13}NiGe$, $MnNi_{0.8}Fe_{0.2}Ge$, $MnNi_{0.77}Fe_{0.23}Ge$, and $Mn_{0.91}Fe_{0.09}NiGe$, respectively (Table S1, ESI†). As a typical display, Fig. 3d shows the comparison between the measured $\Delta L/L$ and the calculated $(\Delta L/L)_0 = (\Delta V/V)/3$ for $Mn_{0.87}Fe_{0.13}NiGe$. In contrast, the measured $\Delta L/L$ for the bonded MnCoGe-based samples never exceeded the crystallographically calculated isotropic $(\Delta V/V)/3$,[29] *e.g.*, the maximal $\Delta L/L$ of $MnCoGe_{0.99}In_{0.01}$ is lower than 100% (~93%) of the crystallographic value $(\Delta V/V)/3$ (Fig. 3e) owing to the possibly introduced porosities during the bonding process. The broadening of the NTE temperature range of the bonded samples compared to that of the free powders involving a martensitic structural transition is ascribed to the introduced residual stress during the molding process[29] (see details in ESI VI†). For a single composition, similar enhancements of NTE are also demonstrated (ESI VII†).

For the Fe-doped MnNiGe alloys, the introduced texture due to the large lattice distortion should play a dominant role for the surprisingly giant NTE. To detect the degree of the introduced texture in the bonded samples with different particle sizes, we performed XRD for the top surface of these bonded cylinders (Fig. 3c). Through comparing the diffraction patterns with those from the free powders collected at room temperature, the degree of texture can be quantified.[40] Here, we consider the Bragg peaks of the hexagonal structure in these diffraction patterns to calculate the orientation coefficient (OC) (see details in ESI IV†).

The OC of each crystal plane $(h_ik_il_i)$ can be calculated by the Harris method,[18] as shown below:

$$\mathrm{OC}(h_ik_il_i) = \frac{I(h_ik_il_i)/I_0(h_ik_il_i)}{(1/N)\cdot\sum_{j=1}^{N}\left[I\left(h_jk_jl_j\right)/I_0\left(h_jk_jl_j\right)\right]} \quad (2)$$

Here, N is the number of the considered diffraction peaks (here, $N = 5$, noting only 5 Bragg peaks from the hexagonal structure), $I_0(h_ik_il_i)$ is the peak intensity of the $(h_ik_il_i)$ crystal plane from the free powders, and $I(h_ik_il_i)$ is the one from the top surface of the bonded sample (Fig. 3c). This equation shows that OC is determined by the intensity ratio of the diffraction peaks from the free powders and bonded pellets. For the free powders without orientation, OC = 1 for any crystal plane (Fig. 4a). If one crystal plane is fully orientated (Fig. 4b) (such as a single crystal), OC = 5 for this plane, while OC = 0 for the other four. Also, $1 < \mathrm{OC} < 5$ indicates partial orientation (Fig. 4c). From the calculated OCs (Table S1, ESI†), it can be found that all the bonded MnNiGe samples with Fe doping have preferred orientations along the (110) and (002) crystal planes. OC(110) was 1.93, 1.69, 1.95, and 1.36, while OC(002) was 1.23, 0.96, 1.40, and 1.22 for $Mn_{0.87}Fe_{0.13}NiGe$, $MnNi_{0.8}Fe_{0.2}Ge$, $MnNi_{0.77}Fe_{0.23}Ge$, and $Mn_{0.91}Fe_{0.09}NiGe$, respectively. In contrast, OC approaches 1 for all the crystal planes of MnCoGeIn, indicating the lack of preferred orientations (Table S1, ESI†). In the hexagonal structure, the (110) plane is parallel to the c-axis, while the (002) plane is perpendicular to the c-axis and parallel to the a-axis (Fig. 4d). For Fe-doped MnNiGe (*e.g.*, $Mn_{0.87}Fe_{0.13}NiGe$), the hexagonal lattice expands along the c-axis by 12.01% and contracts along the a-axis by 9.19% upon cooling during the transition (Fig. S2, ESI†). Clearly, the (110) orientation enhances NTE, while the (002) orientation reduces NTE.

To quantify the joint effect of the (110) and (002) orientations on the enhanced $\Delta L/L$ (compared to the crystallographic value $(\Delta L/L)_0$), a numerical simulation was performed (see details in ESI V†), and the result is three-dimensionally plotted in Fig. 5 and Fig. S8b (ESI†). It can be discerned that all the experimental points roughly fall on the simulated curves. As OC(002) = 1 was fixed, the OC(110) orientation would dominate the thermal expansion, and $(\Delta L/L)/(\Delta L/L)_0$ increased monotonously with varying OC(110), as shown in Fig. 5, implying the large enhancement in NTE. As for the $MnCoGe_{0.99}In_{0.01}$ alloy lacking a preferred orientation, OC approaches 1 for any crystal plane (Table S1, ESI†), and the experimental $(\Delta L/L)/(\Delta L/L)_0$ is smaller than 1 ($\sim$0.93).[29] Obviously, it is more difficult to introduce texture into $MnCoGe_{0.99}In_{0.01}$ as compared to Fe-doped MnNiGe. The crucial cause lies in the different lattice distortions owing to the distinct magnetic structure in martensite for the two alloys.

MnNiGe alloys with different Fe dopings in the present work showed similar lattice distortions owing to their similar cone-spiral magnetic structures (see ESI II and Fig. S3–S5, ESI†). However, their average particle sizes before bonding were different, *i.e.*, 60–80 μm, 20–50 μm, 20–40 μm, and 10–20 μm for $Mn_{0.87}Fe_{0.13}NiGe$, $MnNi_{0.8}Fe_{0.2}Ge$, $MnNi_{0.77}Fe_{0.23}Ge$, and $Mn_{0.91}Fe_{0.09}NiGe$, respectively. Generally, the degree of texture diminishes on reducing the particle size. This rule also works in the present work. One can notice the positive correlation between NTE and the particle size (Fig. 3a and b).

Theoretically, during the process of phase transition accompanied by significant lattice distortion, cracks are produced inside the grains in addition to the dislocations at the grain boundaries. The produced cracks inside the grains must be positively correlated with the degree of lattice distortion during the phase transition. The larger the distortion, the more the cracks appearing in the grains. With the assistance of massive cracks, materials with large distortions prefer cleavage.[41] The right panel of Fig. 5 shows the comparison of the SEM images of a fractured surface between the bulk $Mn_{0.87}Fe_{0.13}NiGe$ (Ni1)

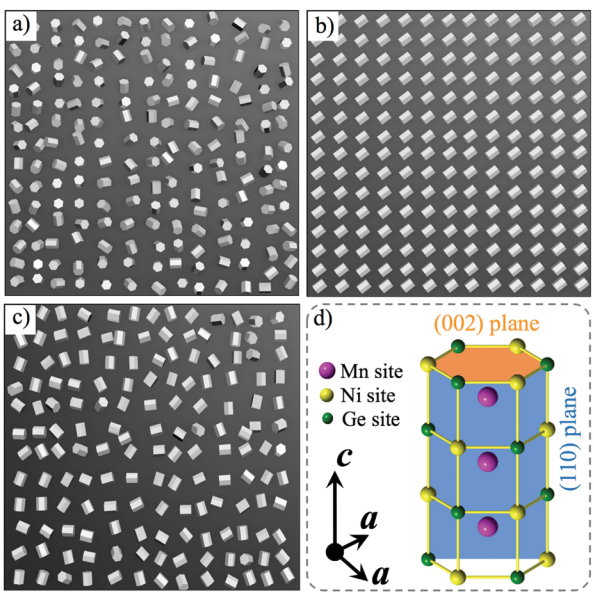

Fig. 4 The sketch of the sample with different textures for the hexagonal structure (space group: $P6_3/mmc$). (a) Free powders without texture, OC = 1 for any crystal plane, (b) fully orientated (110) plane with OC(110) = 5, (c) partially orientated (110) plane with $1 < \mathrm{OC}\ (110) < 5$, (d) schematic diagram of the hexagonal lattice, where the (110) and (002) planes are denoted by blue and yellow, respectively.

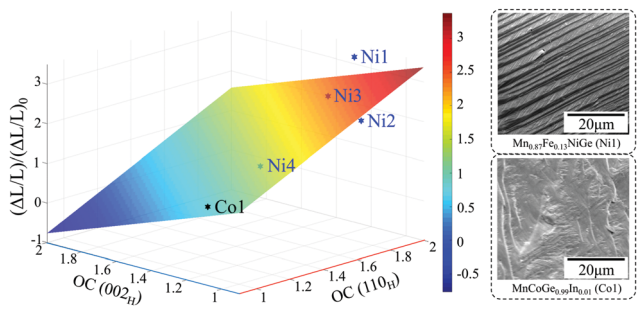

Fig. 5 Left panel: The functional plane drawn according to numerical simulation, where the OC(110), OC(002), and $(\Delta L/L)/(\Delta L/L)_0$ are set as x, y and z, respectively. Stars denote the experimental points for $Mn_{0.87}Fe_{0.13}NiGe$ (Ni1), $MnNi_{0.8}Fe_{0.2}Ge$ (Ni2), $MnNi_{0.77}Fe_{0.23}Ge$ (Ni3), $Mn_{0.91}Fe_{0.09}NiGe$ (Ni4), and $MnCoGe_{0.99}In_{0.01}$ (Co1). Right panel: The typical comparison of SEM micrographs between $Mn_{0.87}Fe_{0.13}NiGe$ (Ni1) and $MnCoGe_{0.99}In_{0.01}$ (Co1) bulk.

and $MnCoGe_{0.99}In_{0.01}$ (Co1). For the former, a clear texture forms along the cleavage plane owing to the larger lattice distortion. In contrast, for the latter, the smaller lattice distortion is not enough to produce enough cracks to promote cleavage. Hence, $MnCoGe_{0.99}In_{0.01}$ tends to randomly break and no obvious texture appears.

During the cleavage process, the cracks tend to cleave the crystal by propagating in the cleavage planes. In the Griffith model,[41] for a crack with length c, the critical stress σ to expand the crack is denoted by the equation $\sigma = \{(2\gamma E)/(\pi c)\}^{1/2}$, where the Young's modulus E is related to the atomic bond strength. Thus, the critical stress σ is proportional to the surface energy γ of the cleaved plane and positively correlates with the bond strength. In a hexagonal crystal, the cleavage planes parallel to the [001] direction, *i.e.*, the *c*-axis have relatively low energy and weak bond strength;[41] hence, the hexagonal crystal tends to cleave along the *c*-axis. Moreover, the *c*-axis prefers to be parallel to the top surface of the bonded pellet under physical pressure during the molding process (Fig. 4b, c and d). As a result, a controlled texture effect appears and a large enhancement in linear $\Delta L/L$ occurs.

Conclusions

By utilizing the large lattice distortion caused by incommensurate cone-spiral magnetic ordering and the constructed texture during the molding process, giant NTE exceeding the average crystallographical contribution was realized in Fe-doped MnNiGe alloys. The maximal $\Delta L/L \sim 23\,690 \times 10^{-6}$ and the corresponding NTE coefficient $\bar{\alpha} \sim -121.5 \times 10^{-6}$ K^{-1} over a wide interval ~195 K (80–275 K) were observed, and the value was 3.3 times larger than that of the corresponding average crystallographical contribution. Neutron powder diffraction and first-principles calculations disclosed the incommensurate cone-spiral magnetic ordering in Fe-doped MnNiGe, which produced a large lattice distortion during the phase transition and motivated the cleavage of the hexagonal phase along the *c*-axis. As a result, a controlled texture effect along the (110) crystal plane appeared, which greatly enhanced the in-plane isotropic linear $\Delta L/L$. The fundamental advancement by utilizing the magnetic structure controlled lattice distortion and the induced texture effect to gain giant NTE paves a new way for exploring NTE materials, which is of great significance for developing novel NTE materials to meet various needs in modern industries, particularly for compensating materials with extremely high PTE coefficients such as the widely used organic or plastic materials.

Author contributions

F. X. H., Q. Z. H., L. H. H. and B. G. S. conceived the study. The first two authors F. R. S. and H. B. Z. contribute equally to this work. F. R. S., H. B. Z., F. X. L. and Z. B. Y. prepared the samples and measured the NTE. Q. Z. H., L. H. H., F. R. S., H. W., J. C. and T. J. L. performed NPD measurements and analysis. J. T. W., S. H. D. and B. T. W. performed DFT calculations. F. R. S., H. B. Z. and J. Z. H. performed magnetic, XRD and SEM measurements. All authors contributed to the analysis and discussion. F. X. H., F. R. S. and J. W. wrote and edited the paper. J. R. S. and B. G. S. made valuable comments on the paper.

Conflicts of interest

There are no conflicts to declare.

Acknowledgements

This work was supported by the National Key Research and Development Program of China (2017YFB0702702, SQ2019YFA070055, 2018YFA0305704, 2016YFB700903, 2017YFA0303601, and 2017YFA0206300), the National Natural Sciences Foundation of China (U1832219, 51531008, 51771223, 51590880, 11674378, 51971240, 11934016, 11674364, and 11974387), the Strategic Priority Research Program (B) and key program of the Chinese Academy of Sciences (CAS).

Notes and references

1 J. Chen, L. Hu, J. X. Deng and X. R. Xing, *Chem. Soc. Rev.*, 2015, **44**, 3522–3567.
2 T. A. Mary, J. S. O. Evans, T. Vogt and A. W. Sleight, *Science*, 1996, **272**, 90–92.
3 J. S. O. Evans, T. A. Mary, T. Vogt, M. A. Subramanian and A. W. Sleight, *Chem. Mater.*, 1996, **8**, 2809–2823.
4 J. Chen, Q. L. Gao, A. Sanson, X. X. Jiang, Q. Z. Huang, A. Carnera, C. G. Rodriguez, L. Olivi, L. Wang, L. Hu, K. Lin, Y. Ren, Z. S. Lin, C. Wang, L. Gu, J. X. Deng, J. P. Attfield and X. R. Xing, *Nat. Commun.*, 2017, **8**, 14441.
5 L. Hu, J. Chen, A. Sanson, H. Wu, C. G. Rodriguez, L. Olivi, Y. Ren, L. L. Fan, J. X. Deng and X. R. Xing, *J. Am. Chem. Soc.*, 2016, **138**, 8320–8323.
6 L. Hu, J. Chen, L. L. Fan, Y. Ren, Y. C. Rong, Z. Pan, J. X. Deng, R. B. Yu and X. R. Xing, *J. Am. Chem. Soc.*, 2014, **136**, 13566–13569.
7 J. Chen, X. R. Xing, G. R. Liu, J. H. Li and Y. T. Liu, *Appl. Phys. Lett.*, 2006, **99**, 101914.
8 J. Chen, X. R. Xing, C. Sun, P. H. Hu, R. B. Yu, X. W. Wang and L. H. Li, *J. Am. Chem. Soc.*, 2008, **130**, 1144–1145.
9 P. H. Hu, J. Chen, J. X. Deng and X. R. Xing, *J. Am. Chem. Soc.*, 2010, **132**, 1925–1928.
10 K. Takenaka and H. Takagi, *Appl. Phys. Lett.*, 2005, **87**, 261902.
11 S. H. Deng, Y. Sun, H. Wu, Q. Z. Huang, J. Yan, K. W. Shi, M. I. Malik, H. Q. Lu, L. Wang, R. J. Huang, L. F. Li and C. Wang, *Chem. Mater.*, 2015, **27**, 2495–2501.
12 C. Wang, L. H. Chu, Q. R. Yao, Y. Sun, M. M. Wu, L. Ding, J. Yan, Y. Y. Na, W. H. Tang, G. N. Li, Q. Z. Huang and J. W. Lynn, *Phys. Rev. B: Condens. Matter Mater. Phys.*, 2012, **85**, 220103.
13 Y. Sun, C. Wang, Y. C. Wen, L. H. Chu, H. Pan and M. Nie, *J. Am. Ceram. Soc.*, 2010, **93**, 2178–2181.
14 P. Tong, D. Louca, G. King, A. Llobet, J. C. Lin and Y. P. Sun, *Appl. Phys. Lett.*, 2013, **102**, 041908.

15 S. P. Li, R. J. Huang, Y. Q. Zhao, W. Wang, Y. M. Han and L. F. Li, *Adv. Funct. Mater.*, 2017, **27**, 1604195.
16 R. J. Huang, Y. Y. Liu, W. Fan, J. Tan, F. R. Xiao, L. H. Qian and L. F. Li, *J. Am. Chem. Soc.*, 2013, **135**, 11469–11472.
17 Y. Z. Song, J. Chen, X. Z. Liu, C. W. Wang, J. Zhang, H. Liu, H. Zhu, L. Hu, K. Lin, S. T. Zhang and X. R. Xing, *J. Am. Chem. Soc.*, 2018, **140**, 602–605.
18 M. Azuma, W. T. Chen, H. Seki, M. Czapski, S. Olga, K. Oka, M. Mizumaki, T. Watanuki, N. Ishimatsu, N. Kawamura, S. Ishiwata, M. G. Tucker, Y. Shimakawa and J. P. Attfield, *Nat. Commun.*, 2011, **2**, 347.
19 X. G. Zheng, H. Kubozono, H. Yamada, K. Kato, Y. Ishiwata and C. N. Xu, *Nat. Nanotechnol.*, 2008, **3**, 724–726.
20 J. Chen, L. L. Fan, Y. Ren, Z. Pan, J. X. Deng, R. B. Yu and X. R. Xing, *Phys. Rev. Lett.*, 2013, **110**, 115901.
21 X. Y. Song, Z. H. Sun, Q. Z. Huang, M. Rettenmayr, X. M. Liu, M. Seyring, G. N. Li, G. H. Rao and F. X. Yin, *Adv. Mater.*, 2011, **23**, 4690–4694.
22 Q. Li, H. Zhu, L. R. Zheng, L. L. Fan, N. Wang, Y. C. Rong, Y. Ren, J. Chen, J. X. Deng and X. R. Xing, *Nano Lett.*, 2017, **17**, 7892–7896.
23 Q. Li, H. Zhu, L. R. Zheng, L. L. Fan, Y. Ren, J. Chen, J. X. Deng and X. R. Xing, *Adv. Sci.*, 2016, **3**, 1600108.
24 H. Zhu, Q. Li, Y. Ren, L. L. Fan, J. Chen, J. X. Deng and X. R. Xing, *Adv. Mater.*, 2016, **28**, 6894–6899.
25 L. Hu, F. Y. Qin, A. Sanson, L. F. Huang, Z. Pan, Q. Li, Q. Sun, L. Wang, F. M. Guo, U. Aydemir, Y. Ren, C. J. Sun, J. X. Deng, G. Aquilanti, J. M. Rondinelli, J. Chen and X. R. Xing, *J. Am. Chem. Soc.*, 2018, **140**, 4477–4480.
26 T. F. Qi, O. B. Korneta, S. Parkin, L. E. De Long, P. Schlottmann and G. Cao, *Phys. Rev. Lett.*, 2010, **105**, 177203.
27 K. Takenaka, Y. Okamoto, T. Shinoda, N. Katayama and Y. Sakai, *Nat. Commun.*, 2017, **8**, 14102.
28 V. Johnson, *Inorg. Chem.*, 1975, **14**, 1117–1120.
29 Y. Y. Zhao, F. X. Hu, L. F. Bao, J. Wang, H. Wu, Q. Z. Huang, R. R. Wu, Y. Liu, F. R. Shen, H. Kuang, M. Zhang, X. Q. Zheng, J. R. Sun and B. G. Shen, *J. Am. Chem. Soc.*, 2015, **137**, 1746–1749.
30 R. R. Wu, L. F. Bao, F. X. Hu, H. Wu, Q. Z. Huang, J. Wang, X. L. Dong, G. N. Li, J. R. Sun, F. R. Shen, T. Y. Zhao, X. Q. Zheng, L. C. Wang, Y. Liu, W. L. Zuo, Y. Y. Zhao, M. Zhang, X. C. Wang, C. Q. Jin, G. H. Rao, X. F. Han and B. G. Shen, *Sci. Rep.*, 2015, **5**, 18027.
31 S. Anzai and K. Ozawa, *Phys. Rev. B: Condens. Matter Mater. Phys.*, 1978, **18**, 2173–2178.
32 Z. Gercsi and K. G. Sandeman, *Phys. Rev. B: Condens. Matter Mater. Phys.*, 2010, **81**, 224426.
33 Z. Gercsi, K. Hono and K. G. Sandeman, *Phys. Rev. B: Condens. Matter Mater. Phys.*, 2011, **83**, 174403.
34 W. Bazela, A. Szytula, J. Todorovic, Z. Tomkowicz and A. Zieba, *Phys. Status Solidi A*, 1976, **38**, 721.
35 A. Szytula, A. T. Pedziwiatr, Z. Tomkowicz and W. Bazela, *J. Magn. Magn. Mater.*, 1981, **25**, 176–186.
36 E. K. Liu, W. H. Wang, L. Feng, W. Zhu, G. J. Li, J. L. Chen, H. W. Zhang, G. H. Wu, C. B. Jiang, H. B. Xu and D. B. Frank, *Nat. Commun.*, 2012, **3**, 873.
37 W. Bazela, A. Szytula, J. Todorovic and A. Zieba, *Phys. Status Solidi A*, 1981, **64**, 367–378.
38 J. P. Perdew and Y. Wang, *Phys. Rev. B: Condens. Matter Mater. Phys.*, 1992, **45**, 13244–13249.
39 S. H. Deng, Y. Sun, L. Wang, Z. X. Shi, H. Wu, Q. Z. Huang, J. Yan, K. W. Shi, P. W. Hu, A. Zaoui and C. Wang, *J. Phys. Chem. C*, 2015, **119**, 24983–24990.
40 G. B. Harris, *Philos. Mag.*, 1952, **43**, 113–123.
41 B. Siemens, C. Domke, P. Ebert and K. Urban, *Phys. Rev. B: Condens. Matter Mater. Phys.*, 1999, **59**, 3000–3007.

